

# Comparison and visualization of focusing wave fields from various time reversal techniques in elastic media

Brian E. Anderson,<sup>a)</sup> Timothy J. Ulrich, and Pierre-Yves Le Bas

*Geophysics Group (EES-17), MS D443, Los Alamos National Laboratory, Los Alamos,  
New Mexico 87545*

*bea@lanl.gov, tju@lanl.gov, pylb@lanl.gov*

**Abstract:** This Letter presents a series of time reversal experiments conducted on the surface of a fused silica glass block. Four different time reversal techniques are compared using three different imaging conditions. The techniques include two classical time reversal experiments: one with a pulse waveform source and one with an impulse response generated from a chirp signal. The other two techniques utilize the deconvolution, or inverse filter, signal processing methods for obtaining the signals to back propagate using a pulse waveform and an impulse response from a chirp. The max-in-time, symmetry, and energy current imaging conditions are compared.

© 2013 Acoustical Society of America

**PACS numbers:** 43.60.Tj, 43.40.Le, 43.35.Zc [DC]

**Date Received:** March 12, 2013    **Date Accepted:** October 22, 2013

## 1. Introduction

Time reversal (TR) is a wave focusing technique used to locate unknown sources or to intentionally create high intensity focusing of sound at a desired location.<sup>1,2</sup> The TR experiments presented here require a source transducer to broadcast wave energy that propagates through a medium where a laser vibrometer measures the out-of-plane vibration at a selected location. The signal recorded by the laser vibrometer is then reversed in time and the reversed signal is broadcast from the source transducer, which then produces a focusing of energy at the laser vibrometer location. An increase in the focal amplitude and improvement of the spatial focusing quality may be obtained by using more source transducers and/or recording more reflections of energy at the laser location, however, the recording of the wave energy produced by each source transducer should be done individually.

In this Letter, we present a series of experiments carried out on the surface of a glass block to compare the quality of the focusing of four variants of the TR technique. We also use three different imaging conditions in this comparison. The purpose of this letter is to compare the four different techniques and compare the virtues of the imaging conditions to determine the best technique and imaging condition to use for TR experiments. TR techniques are used in solid samples for nondestructive evaluation<sup>3-8</sup> including localization of acoustic emissions, crack detection, and scatterer/disbonding localization, and they are used for material characterization<sup>9</sup> and electronic touch panels.<sup>10</sup> Though the conclusions drawn from these experiments directly relate to TR experiments conducted only on solid blocks of material with elastic waves, the authors expect similar conclusions to be drawn in reverberant cavities with acoustic waves and may have some insight for experiments conducted in ocean waveguides. Movies of the temporal evolution of these imaging conditions are also provided in the multimedia files, which may be the first experimental visualization of these

---

<sup>a)</sup> Author to whom correspondence should be addressed.

imaging conditions given in the literature. Van Damme *et al.*<sup>11</sup> and Gallot *et al.*<sup>12</sup> have each given snapshot images to visualize the deconvolution technique (or inverse filter technique), but their focus was not to provide a direct comparison of this technique to classical TR techniques nor did they attempt to provide visualizations of various imaging conditions. The authors believe that there is a fair amount of physical insight to gain about the various TR signal processing techniques and the imaging conditions used from viewing these movies.

## 2. Experiment setup

A fused silica glass block of dimensions 10 cm<sup>3</sup> is used for the experiments (mass density of 2210 kg/m<sup>3</sup> and surface wave speed of 3780 m/s). A set of eight 12.7 mm diameter piezoelectric transducers were bonded (using epoxy) onto the block at random locations. A Polytec (Waldbronn, Germany) OFV-303, out-of-plane, laser vibrometer is used to create a virtual source<sup>13</sup> at a selected location on one of the surfaces of the block. The same vibrometer is used in conjunction with a dual-axis positioning system to allow the wave fields on the surface of the block (containing the virtual source) to be scanned as the experiments are repeated at each scan location. The vibrometer scanned an area spanning 80 mm<sup>2</sup> with a 1 mm step size and the virtual source located at ( $x_{vs} = 40$  mm,  $y_{vs} = 40$  mm). The block sample is pictured in Fig. 2(a) of Ref. 14 (though a larger piece of reflective tape was applied for these experiments to enhance the reflectivity of the laser). Signals were generated and acquired with a sampling frequency of 10 MHz, a 32 768 point time span (3.2768 ms), a 12-bit D/A converter card for the source signal, a 14-bit A/D converter card for the recording of signals from the laser vibrometer, and 244 synchronous averages. The normalized signals sent to the transducers had a peak to peak voltage of 100 V for both forward and backward signals in order to maximize the energy broadcast for our amplifier. It should be noted here that the transducers have a significant resonance around 200 kHz resulting from a radial resonant motion of the transducer disks, thus unless corrected for by using the deconvolution operation for example, the TR results will be fairly narrowband in their frequency spectra. The experimental setup employed here essentially maximizes the quality of the focusing from the four TR methods used since the eight channels and long amount of coda (time over which the forward propagation is recorded) allow for reverberant sampling of the entire sample.

The first type of TR technique, which we refer to as the classical pulse method (CPM), employed a 200 kHz sinusoidal pulse (with a  $\sin^2$  envelope applied) of pulse width 10  $\mu$ s. This pulse was then centered in the 3.2768 ms time window. The source signal was broadcast from each transducer individually and the velocity responses at ( $x_{vs}, y_{vs}$ ) were recorded by the laser. Each of these forward signals,  $r_{i,cp}$ , were then reversed in time and simultaneously broadcast from the respective transducers used to create them, creating a focus of energy at ( $x_{vs}, y_{vs}$ ).

The second type of TR technique, which we refer to as the classical chirp method (CCM), employed a linear chirp signal spanning 0–400 kHz beginning at time 0 and ending at time 3.0000 ms. A 400 kHz bandwidth was selected, as that represents the bandwidth, measured from null to null of the main lobe for the spectrum of the pulse used in the CPM. Each transducer broadcasts this chirp signal individually and the velocity responses are recorded by the laser at ( $x_{vs}, y_{vs}$ ). A cross correlation of the source signal and the laser velocity signals was then performed to obtain the band limited impulse responses,  $r_{i,cc}$ , between each transducer and ( $x_{vs}, y_{vs}$ ). These impulse responses were then zero padded from time 0 to time 1.6384 ms, and then the first 1.6384 ms of the impulse response was kept for the second half of the source signal window in order to center the focus of energy in the recorded time window. The signals,  $r_{i,cc}$ , were then reversed in time and simultaneously broadcast from the respective transducers used to create them, creating a focus of energy at ( $x_{vs}, y_{vs}$ ).

The third type of TR technique, which we refer to as the deconvolution pulse method (DPM), used the deconvolution operation (or inverse filter operation)<sup>11,12,15,16</sup>

on  $r_{i,cp}$  to create the inverse filtered signals,  $r_{i,dp}$ . The  $r_{i,dp}$  signals were reversed in time and simultaneously broadcast from the respective transducers used to create them, creating a focus of energy at  $(x_{vs}, y_{vs})$ .

The fourth type of TR technique, which we refer to as the deconvolution chirp method (DCM), used the deconvolution operation on  $r_{i,cc}$ , which produced the inverse filtered signals,  $r_{i,dc}$ . The  $r_{i,dc}$  signals were reversed in time and simultaneously broadcast from the respective transducers used to create them, creating a focus of energy at  $(x_{vs}, y_{vs})$ .

It should be noted that the forward propagation velocities for the pulse and chirp methods were approximately 0.2 mm/s peak to peak and 2 mm/s peak to peak, respectively. This illustrates why the chirp method is advantageous in providing cleaner signals for TR. The focal amplitudes for the classical and deconvolution TR techniques (whether the pulse or chirp method is used) were approximately 20 mm/s peak to peak and 10 mm/s peak to peak, respectively. It is well known that the deconvolution techniques improve the bandwidth of the signal because they reduce the overall focal amplitude.<sup>16</sup>

### 3. Discussion

Figure 1 displays the square of the instantaneous, out-of-plane velocity wave field at the peak time of focus (the center of the time window, 1.6384 ms) for each of the four TR techniques used to focus energy (we square the wave fields for a proper comparison to the symmetry and energy current imaging conditions). In Figs. 1(a) and 1(b), note the ring shaped wave fronts surrounding the focal point with the classical pulse and classical chirp TR techniques (it is more obvious to observe these rings in the movie version of this figure). Contrast those images with the results from the deconvolution techniques in Figs. 1(c) and 1(d) where the energy is clearly concentrated only at the focal location and has less energy away from the focal location. It should also be noted that the classical techniques yield focal spot maximum amplitudes that are nearly twice as large as the respective values using deconvolution techniques. The deconvolution results are also narrower spatially than the classical results. A four panel movie showing the progression of the wave fields over time may be found in [Mm. 1](#) (from  $t = T/2 - 300$  ms to  $t = T/2 + 200$  ms). Another movie of this same data

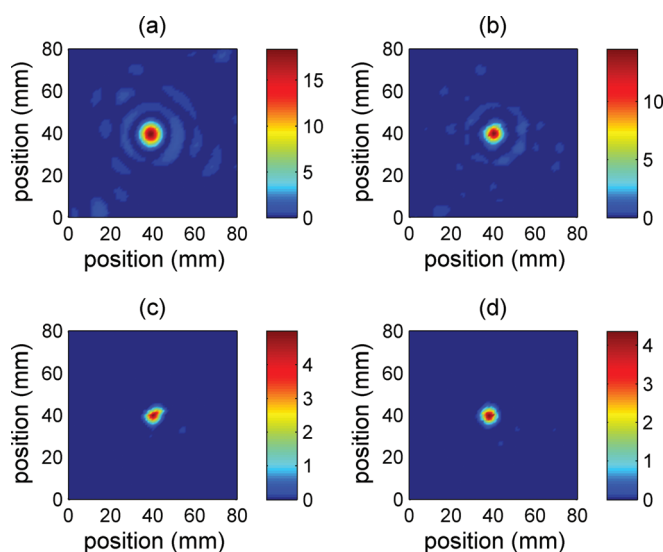


Fig. 1. Instantaneous velocity spatial maps at the time of focus for the (a) CPM, (b) CCM, (c) DPM, and (d) DCM.

showing the square of the instantaneous wave fields (similar to how the data is displayed in Fig. 1) may be found in Mm. 2 We include the wave field movie so that physical insight may be gained from observing the motion of the wave fronts that create the focal signals. The movie shows that the deconvolution techniques create a single, spherical, incident wave front that produces a tight focusing in time, whereas the classical techniques create a focusing wave field that is not compressed in time and instead a series of wave fronts coalesce at  $(x_{vs}, y_{vs})$ . The series of coalescing wave fronts is a result of the transducer response which colors the focal signal. Fortunately, the deconvolution processing corrects for the transducer response and thus allows for the sharper focus. The CCM result shows finer spatial features than the CPM since it provides a greater signal-to-noise ratio for the higher frequencies than the CPM allows.

**Mm. 1.** Video of the progression of the wave fields for the following time reversal techniques: CPM, CCM, DPM, and DCM. This is a file of type “mpg” (5.5 MB).

**Mm. 2.** Video of the progression of the squared wave fields for the following time reversal techniques: CPM, CCM, DPM, and DCM. This is a file of type “mpg” (5.5 MB).

The well known max-in-time imaging condition,  $I_{MT}$ , is described by

$$I_{MT}(x, y) = \max_{t \in [0, T]} \{|v(x, y, t)|\}, \quad (1)$$

where  $T$  is the signal length (3.2768 ms) and  $v(x, y, t)$  is the out-of-plane velocity signal acquired by the laser vibrometer at each scan location  $(x, y)$ . Thus with the  $I_{MT}$ , the values at each  $(x, y)$  location are not necessarily simultaneous in time. Figure 2 displays the  $(I_{MT})^2$  for each TR technique (we square the  $I_{MT}$  for a proper comparison to the symmetry and energy current imaging conditions). Similar observations about the results in Fig. 1 can be made about the results in Fig. 2 in that the background levels (energy not at the focal locations) are somewhat lower for the deconvolution techniques than for the classical techniques. The  $(I_{MT})^2$  images result in higher background levels than are shown in Fig. 1 for each respective technique as expected.

The symmetry imaging condition,<sup>13</sup>  $I_{SM}(t)$ , is created by taking a signal, or a portion of a signal, and splitting it up into two equal halves and then performing the zero-lag temporal cross correlation of these two halves. Mathematically, this is given

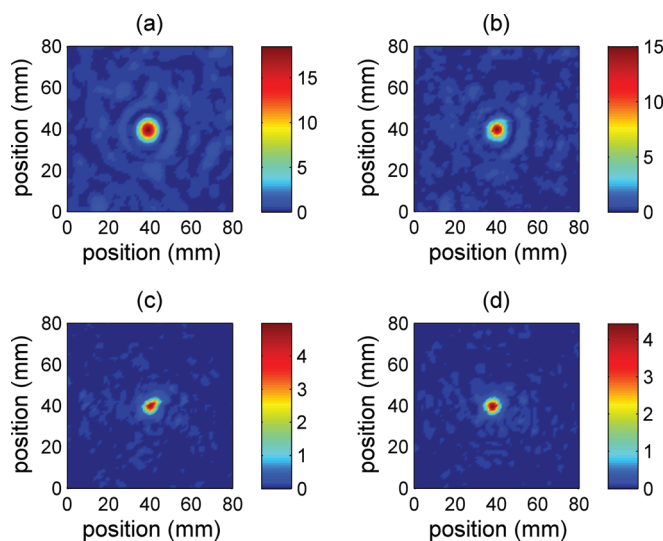


Fig. 2. Max-in-time imaging condition spatial maps for the (a) CPM, (b) CCM, (c) DPM, and (d) DCM.

by Eq. (4) in Ref. 13. Here we use signal lengths of  $T/4$  on either side of each time step for which the imaging condition is created. Figure 3 displays the  $I_{SM}(T/2)$  for each TR technique (this is the imaging condition at the focal time with  $T/4$  signal lengths used on either side of  $T/4$  to compute the instantaneous symmetry wave field). In these results, the CPM yields the highest level of symmetry (darkest red spot), but also has the highest background levels. The deconvolution techniques yield lower background levels than the respective classical techniques and have smaller focal spot sizes. A four panel movie showing the progression of the  $I_{SM}(t)$  fields over time may be found in Mm. 3 (from  $t = T/2 - 300$  ms to  $t = T/2 + 200$  ms). The symmetry condition movies do not evolve in time nearly as rapidly as the movies of the instantaneous wave fields. Near the focal time of the symmetry movies, one can notice that the deconvolution techniques result in sharply defined temporal focusing compared to the classical techniques.

Mm. 3. Video of the progression of the symmetry condition wave fields for the following time reversal techniques: CPM, CCM, DPM, and DCM. This is a file of type “mpg” (5.5 MB).

The energy current imaging condition,<sup>17</sup>  $I_{EC}(t)$ , is created by first computing the energy current density vector wave field, which is essentially the gradient of the instantaneous velocity wave field at  $(x, y)$  multiplied by the time derivative of the velocity wave field at  $(x, y)$  as defined by Eq. (2) in Ref. 17.  $I_{EC}$ , then, is the flux through a closed two-dimensional surface as defined by Eq. (3) in Ref. 17. Figure 4 displays the  $|I_{EC}(T/2)|$  for each TR technique. In comparing the four energy current images, it may be observed that the techniques that utilize a chirp signal yield lower background levels and spatially smaller focal spot sizes than when a pulse is used. It may not be visually clear that the DCM yields the lowest background noise levels of the four techniques, but this conclusion may be determined by closer inspection of the results. A four panel movie showing the progression of the  $I_{EC}(t)$  fields over time may be found in Mm. 4 (from  $t = T/2 - 300$  ms to  $t = T/2 + 200$  ms). Another movie of the  $|I_{EC}(T/2)|$  fields over time is also included (similar to the data displayed in Fig. 4) in Mm. 5. The movies show repeated maxima at the focal location even with the deconvolution techniques corresponding to the maximal convergence or divergence of energy at the focal location. The peak, net flow of energy should occur just before and just after the focal time with a net positive flow of energy inward just before the focal time

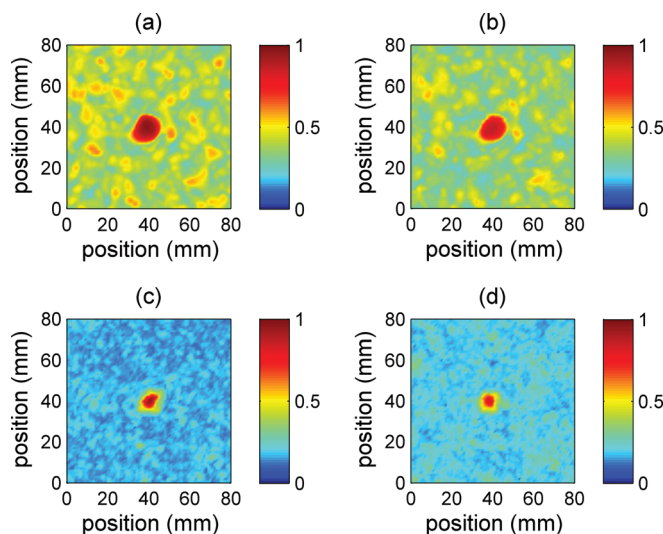


Fig. 3. Symmetry-based imaging condition spatial maps at the time of focus for the (a) CPM, (b) CCM, (c) DPM, and (d) DCM.

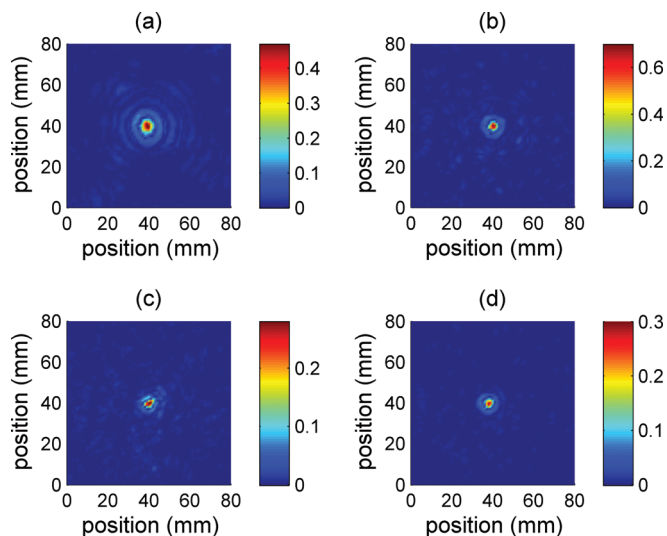


Fig. 4. Energy current imaging condition spatial maps at the time of focus for the (a) CPM, (b) CCM, (c) DPM, and (d) DCM.

and a net negative flow of energy outward just after the focal time, hence, why one would expect multiple maxima at different times.

**Mm. 4.** Video of the progression of the energy current wave fields for the following time reversal techniques: CPM, CCM, DPM, and DCM. This is a file of type “mpg” (5.5 MB).

**Mm. 5.** Video of the progression of the absolute value of the energy current wave fields for the following time reversal techniques: CPM, CCM, DPM, and DCM. This is a file of type “mpg” (5.5 MB).

It is clear from a visual comparison of the energy current results to the results using other imaging conditions that the  $I_{EC}$  images yield the smallest focal spot sizes, irrespective of the TR technique used. Also, the  $I_{SM}$  images have smaller focal spot sizes than the  $I_{MT}$  images. However, the background levels for the  $I_{MT}$  images are slightly lower than for the  $I_{EC}$  images (as also determined in Ref. 17) and much lower than for the  $I_{SM}$  images (as also determined in Ref. 13). Computationally, the  $I_{MT}$  is the quickest imaging metric to compute since it requires only a maximum value operation over the time signal for each evaluation location. The  $I_{SM}$  imaging metric takes a longer amount of time to compute as it requires a cross correlation of two signals for each evaluation location. The  $I_{EC}$  imaging metric takes the longest amount of time to compute as it requires instantaneous velocity spatial maps to be created in order to compute the gradient, and then a multiplication of the gradient field of one time step and the next time step is required for each evaluation location.

#### 4. Conclusions

We have shown in these experiments that, in general, the deconvolution techniques lead to sharper concentrations of energy at the focal location than the classical techniques in terms of the relative background levels and the focal spot sizes for any imaging condition. The movie results also show that the deconvolution results yield sharper foci temporally (resulting from a single incident wave front in these experiments). The temporal sharpness of the foci using the deconvolution operation stems from the operation’s ability to correct for the added ringing that results from the inherent narrow-band frequency response of the piezoelectric transducers used. Irrespective of the TR technique used, it is clear that the energy current imaging condition yields the smallest focal spot sizes spatially. The background levels are lowest for the max-in-time imaging

condition of the three imaging conditions compared here. There exists a tradeoff in the use of a deconvolution technique versus a classical technique such that the focal spot amplitude is reduced by about 1/2 in these experiments relative to the classical techniques, although the deconvolution techniques generally offer a tighter spot size and lower background levels. In TR applications where source reconstruction is desired, such as earthquake localization and communications applications, a tighter focus in space and time is desired to accurately locate the source and reconstruct the source's temporal output, although reduced focal amplitude can be a critical problem for long range communications. On the contrary, when the application of TR is used to maximally focus energy at a certain location such as for acoustic lithotripsy and nondestructive damage detection, the larger amount of energy may be much more important than the spatial extent of the focus and the tight temporal concentration of energy. In fact, higher energy over a longer period of time may even be desirable for these later applications.

### Acknowledgment

This research was supported by institutional support (LDRD) at the Los Alamos National Laboratory.

### References and links

- <sup>1</sup>M. Fink, "Time reversed acoustics," *Phys. Today* **50**, 34–40 (1997).
- <sup>2</sup>B. E. Anderson, M. Griffa, C. Larmat, T. J. Ulrich, and P. A. Johnson, "Time reversal," *Acoust. Today* **4**(1), 5–16 (2008).
- <sup>3</sup>T. J. Ulrich, A. M. Sutin, T. Claytor, P. Papin, P.-Y. Le Bas, and J. A. TenCate, "The time reversed elastic nonlinearity diagnostic applied to evaluation of diffusion bonds," *Appl. Phys. Lett.* **93**, 151914 (2008).
- <sup>4</sup>B. E. Anderson, M. Griffa, P.-Y. Le Bas, T. J. Ulrich, and P. A. Johnson, "Experimental implementation of reverse time migration for nondestructive evaluation applications," *J. Acoust. Soc. Am.* **129**(1), EL8–EL14 (2011).
- <sup>5</sup>S. Dos Santos and Z. Prevorovsky, "Imaging of human tooth using ultrasound based chirp-coded nonlinear time reversal acoustics," *Ultrasonics* **51**(6), 667–674 (2011).
- <sup>6</sup>P.-Y. Le Bas, T. J. Ulrich, B. E. Anderson, R. A. Guyer, and P. A. Johnson, "Probing the interior of a solid volume with time reversal and nonlinear elastic wave spectroscopy," *J. Acoust. Soc. Am.* **130**(4), EL258–EL263 (2011).
- <sup>7</sup>L. Quan, X. Liu, and X. Gong, "Nonlinear nonclassical acoustic method for detecting the location of cracks," *J. Appl. Phys.* **112**(5), 054906 (2012).
- <sup>8</sup>A. S. Gliozzi, M. Scalerandi, and P. Antonaci, "One-channel time reversal acoustics in highly attenuating media," *J. Phys. D: Appl. Phys.* **46**(13), 135502 (2013).
- <sup>9</sup>J. Brum, S. Catheline, N. Benech, and C. Negreira, "Shear elasticity estimation from surface wave: The time reversal approach," *J. Acoust. Soc.* **124**(6), 3377–3380 (2008).
- <sup>10</sup>M. R. Bai and Y. K. Tsai, "Impact localization combined with haptic feedback for touch panel applications based on the time-reversal approach," *J. Acoust. Soc. Am.* **129**(3), 1297–1305 (2011).
- <sup>11</sup>B. Van Damme, K. Van Den Abeele, Y. Li, and O. Bou Matar, "Time reversed acoustics techniques for elastic imaging in reverberant and nonreverberant media: An experimental study of the chaotic cavity transducer concept," *J. Appl. Phys.* **109**(10), 104910 (2011).
- <sup>12</sup>T. Gallot, S. Catheline, P. Roux, and M. Campillo, "A passive inverse filter for Green's function retrieval," *J. Acoust. Soc. Am.* **131**(1), EL21–EL27 (2012).
- <sup>13</sup>T. J. Ulrich, M. Griffa, and B. E. Anderson, "Symmetry-based imaging condition in time reversed acoustics," *J. Appl. Phys.* **104**(6), 064912 (2008).
- <sup>14</sup>B. E. Anderson, T. J. Ulrich, M. Griffa, P.-Y. Le Bas, M. Scalerandi, A. S. Gliozzi, and P. A. Johnson, "Experimentally identifying masked sources applying time reversal with the selective source reduction method," *J. Appl. Phys.* **105**(8), 083506 (2009).
- <sup>15</sup>M. Tanter, J. F. Aubry, J. Gerber, J. L. Thomas, and M. Fink, "Optimal focusing by spatiotemporal inverse filter. I. Basic principles," *J. Acoust. Soc. Am.* **110**(1), 37–47 (2001).
- <sup>16</sup>T. J. Ulrich, B. E. Anderson, P.-Y. Le Bas, C. Payan, J. Douma, and R. Snieder, "Improving time reversal focusing through deconvolution: 20 questions," *Proc. Meet. Acoust.* **16**, 045015 (2012).
- <sup>17</sup>B. E. Anderson, R. A. Guyer, T. J. Ulrich, P.-Y. Le Bas, C. Larmat, M. Griffa, and P. A. Johnson, "Energy current imaging method for time reversal in elastic media," *Appl. Phys. Lett.* **95**(2), 021907 (2009).